Laser & Photonics Reviews

LASER & PHOTONICS REVIEWS

www.lpr-journal.org

RESEARCH ARTICLE

Ultra-Transparent Self-Healing Large-Area Hybrid Metal Halide Glass Scintillators for High-Resolution X-ray Imaging

Shilin Jin[1] | Luyao Wei[1] | Zhibin Lin[2] | Yongping Zheng[1] | Qiushui Chen[2] | Daqin Chen[1,3]

[1]College of Physics and Energy, Fujian Normal University, Fuzhou, People's Republic of China | [2]MOE Key Laboratory for Analytical Science of Food Safety and Biology College of Chemistry, Fuzhou University, Fuzhou, People's Republic of China | [3]Fujian Provincial Engineering Technology Research Center of Solar Energy Conversion and Energy Storage, Fuzhou, People's Republic of China

Correspondence: Yongping Zheng (zyp@fjnu.edu.cn) | Daqin Chen (dqchen@fjnu.edu.cn)

Received: 30 April 2026 | **Revised:** 5 August 2026 | **Accepted:** 13 August 2026

Keywords: glasses | hybrid metal halides | luminescent materials | scintillators | X-ray imaging

ABSTRACT

Hybrid metal halide glasses are attractive for next-generation scintillators but typically suffer from limited size, poor stability, and unsustainable processing. Here, we report a large-area Sb: ETP_2MnCl_4 glass scintillator that combines high optical transparency (>92%), light yield of 19,301 photons·MeV^{-1}, detection limit of 82.3 $nGy_{air}·s^{-1}$, and spatial resolution of 30.1 $lp·mm^{-1}$. Structural analyses reveal that Sb: ETP_2MnCl_4 crystal can be melt-quenched into amorphous glass while retaining organic cations and $[MnCl_4]^{2-}$ tetrahedra, thus preserving photophysical properties. Notably, Sb^{3+} introduces strong ultraviolet absorption and dual radiative channels, where self-trapped exciton emission and efficient $Sb^{3+}\rightarrow Mn^{2+}$ energy transfer synergistically enhance PLQY to 90.4%. Under X-ray excitation, the glass exhibits stable Mn^{2+}-dominated radioluminescence, outperforming $Bi_4Ge_3O_{12}$. The 12.9-inch glass screens enable micro-scale static imaging and high-speed angiography on a smartphone platform. Combined with low-temperature reshaping and reversible crystal-glass cycling, Sb: ETP_2MnCl_4 emerges as a scalable, sustainable scintillator for eco-friendly radiation detection and portable medical imaging.

1 | Introduction

X-rays, as high-energy electromagnetic radiation with strong penetration, are widely applied in fields such as space exploration, medical diagnostics, security screening, and industrial non-destructive inspection [1–4]. In these applications, scintillators serve as the essential functional materials that convert X-rays into visible light, with their performance ultimately dictating imaging quality, spatial resolution, and operational stability. Current commercial scintillators are mainly based on inorganic crystals, such as $Bi_4Ge_3O_{12}$ (BGO), $Lu_3Al_5O_{12}$: Ce^{3+} (LuAG: Ce), and CsI: Tl, which feature high X-ray absorption and excellent radiation resistance [5, 6]. However, their synthesis generally requires high temperatures and long cycles, resulting in substantial energy consumption and limited scalability. Then, the fabrication of large-area inorganic single-crystal scintillator screens usually requires precise crystal cutting, surface polishing, and post-processing, which further increases the manufacturing cost and limits shape adaptability. Additionally, some rely on toxic or scarce elements, which raise concerns about sustainability and environmental impact. To overcome these limitations, organic crystal scintillators and inorganic powder/polymer composites have been explored [7–9]. Organic systems are low-cost and solution-processable, but they lack sufficient X-ray blocking due to their low atomic numbers. Composite scintillators, produced by dispersing inorganic powders into polymer matrices, improve absorption but often face severe light scattering, particle agglomeration, and interfacial inhomogeneity, leading to poor transparency and degraded spatial resolution.

All rights reserved, including rights for text and data mining and training of artificial intelligence technologies or similar technologies.
© 2026 Wiley-VCH GmbH

Organic-inorganic hybrid metal halides (OIMHs) have recently emerged as promising alternatives, combining high-Z metal-halide clusters (e.g., Sb-Cl/Br, Mn-Cl/Br, Cu-Br/I, Zr-Cl, Eu-Cl/Br/I) with integrated functional organic cations [10–13]. The excellent luminescent properties, high design flexibility, and solution processability make them attractive for scintillation applications [14–16]. Mn(II)-based OIMHs, in particular, have demonstrated near-unity photoluminescence quantum yields (PLQY), efficient radioluminescence (RL) properties, and low environmental toxicity, making them highly attractive as eco-friendly scintillation candidates (Table S1). Nonetheless, achieving large-area, transparent scintillating screens remains a major challenge: powder-polymer composites compromise transparency, while single-crystal growth is difficult to scale.

Glass-state OIMHs prepared via melt-quenching provide a compelling pathway. Their amorphous nature enables high transparency, uniformity, and scalable fabrication into large-area panels, curved screens, or fibers [17, 18]. Unlike in-situ quantum dot glasses, hybrid glasses can be processed at lower temperatures while avoiding concentration limits and self-absorption losses inherent to nanocrystal formation [19]. Furthermore, the incorporation of bulky organic cations with high steric hindrance can effectively suppress crystallization during melt-quenching [20, 21], thereby enabling the bulk preparation of transparent glasses while retaining the luminescent activity of functional inorganic units. This emerging class of hybrid scintillating glass combines optical homogeneity with excellent processability, but its development remains nascent, with unresolved issues of stability and crystallization control. Moreover, in the pursuit of low-carbon and sustainable development, increasing emphasis should be placed on the recyclability of halide glasses to prevent disposable waste, conserve resources, and mitigate potential heavy-metal contamination.

Herein, we report a new large-area, highly transparent, and recyclable hybrid metal halide glass scintillator based on Sb: ETP_2MnCl_4 (ETP^+ = Ethy-ltriphenylphosphonium). Leveraging a low melt-quenching temperature (<220°C), the intrinsic luminescence of $[MnCl_4]^{2-}$ tetrahedra is preserved while enabling bulk glass formation. The deliberate incorporation of a highly sterically hindered Bis(2-diphenylphosphinophenyl)ether (DPEPhos) molecule effectively suppresses crystallization during quenching, yielding optically uniform glasses with over 90% transmittance across the visible spectral range. Using heat-resistant and flexible silicone molds, we further achieve rapid and scalable production of 12.9-inch (21.5 × 28.5 cm^2) transparent scintillation screens with precisely controlled geometry. Compared with conventional inorganic scintillators that usually require high-temperature crystal growth or sintering, this low-temperature melt-quenching route substantially reduces energy input, equipment requirements, and processing time. Moreover, direct mold-assisted shaping enables large-area screens with controllable thickness and geometry without the cutting and polishing steps required for rigid inorganic single crystals. These glasses deliver a high light yield of 19,301 photons·MeV^{-1}, an ultra-low detection limit of 82.3 $nGy_{air}·s^{-1}$, and a spatial resolution up to 30.1 lp·mm^{-1}, enabling not only static micron-scale X-ray imaging but also real-time dynamic tracking of moving objects. Moreover, their intrinsic low-temperature self-healing and recyclability establish a sustainable platform for next-generation, eco-friendly scintillating glass screens.

2 | Results and Discussion

A series of Sb-doped ETP_2MnCl_4 single crystals was synthesized via a hydrothermal method, achieving a PLQY of ~90.4%. Single-crystal X-ray diffraction (SCXRD) analysis revealed that the compound crystallizes in the monoclinic *C1/c1* space group, with lattice parameters of a = 12.2121(2) Å, b = 20.8816(2) Å, c = 16.3751(2) Å, and Z = 4. Crystallographic information and detailed structural parameters are provided in Table S2. As illustrated in Figure 1a, ETP_2MnCl_4 is a typical 0D structure, in which each Mn^{2+} ion is tetrahedrally coordinated by Cl^- to form an isolated $[MnCl_4]^{2-}$. The units are periodically isolated by bulky organic cations, with no direct connections between adjacent tetrahedra, thereby effectively suppressing nonradiative relaxation of excited Mn^{2+} via dipole-dipole and spin-exchange interactions [18, 22]. Figure 1b further illustrates the spatial configuration of the ETP^+ and $[MnCl_4]^{2-}$ moieties. Slight variations in Mn—Cl bond lengths and Cl—Mn—Cl bond angles suggest minor structural distortion within the tetrahedra (Table S3). The inter-unit distances between neighboring $[MnCl_4]^{2-}$ clusters exceed 9.5 Å, while the C—H···Cl hydrogen bond lengths between the organic cations and halide anions range from 2.6 Å to 3.9 Å (Figure S1), indicating very weak coupling among inorganic modules and limited bonding forces at the organic-inorganic interface [2, 22].

Powder XRD (PXRD) patterns of both undoped and Sb-doped ETP_2MnCl_4 closely match the simulated profiles derived from single-crystal data, confirming the high crystallinity and phase purity of the synthesized materials (Figure 1c; Figure S2). For comparison, an ETP_2SbCl_5 crystal was also prepared using the same method. Although it exhibits a similar host-guest structure, the compound crystallizes in the *C2/c* space group, resulting in a markedly different diffraction pattern from that of ETP_2MnCl_4 (Figure S3). Therefore, it is concluded that Sb^{3+} dopants are incorporated into the ETP_2MnCl_4 host by substituting Mn^{2+} sites and forming $[SbCl_4]^-$ units owing to the comparable ionic radii of Sb^{3+} (CN = 4, r = 0.74 Å) and Mn^{2+} (CN = 4, r = 0.60 Å). Energy-dispersive X-ray (EDX) spectroscopy, elemental mapping, and X-ray photoelectron spectroscopy (XPS) further collectively confirmed the chemical composition and verified the presence of Sb dopants in ETP_2MnCl_4 (Figure S4).

Interestingly, Sb: ETP_2MnCl_4 glass, a hybrid luminescence screen characterized by excellent plasticity and high optical transparency, can be further fabricated via a straightforward crystal-melting-quenching or grinding-melting-quenching process (Figure 1d). In practice, either crystalline samples or stoichiometrically mixed precursors are finely ground, transferred into a glass beaker, and heated under continuous stirring until a homogeneous, transparent melt is obtained. The resulting melt is then cast into a predesigned mold and rapidly quenched to room temperature, producing transparent glasses with tunable thickness and shape. This facile, solution-free-assisted approach enables rapid and scalable fabrication, highlighting its strong potential for sustainable industrial application. This low-temperature and mold-assisted process avoids the energy-intensive crystal-

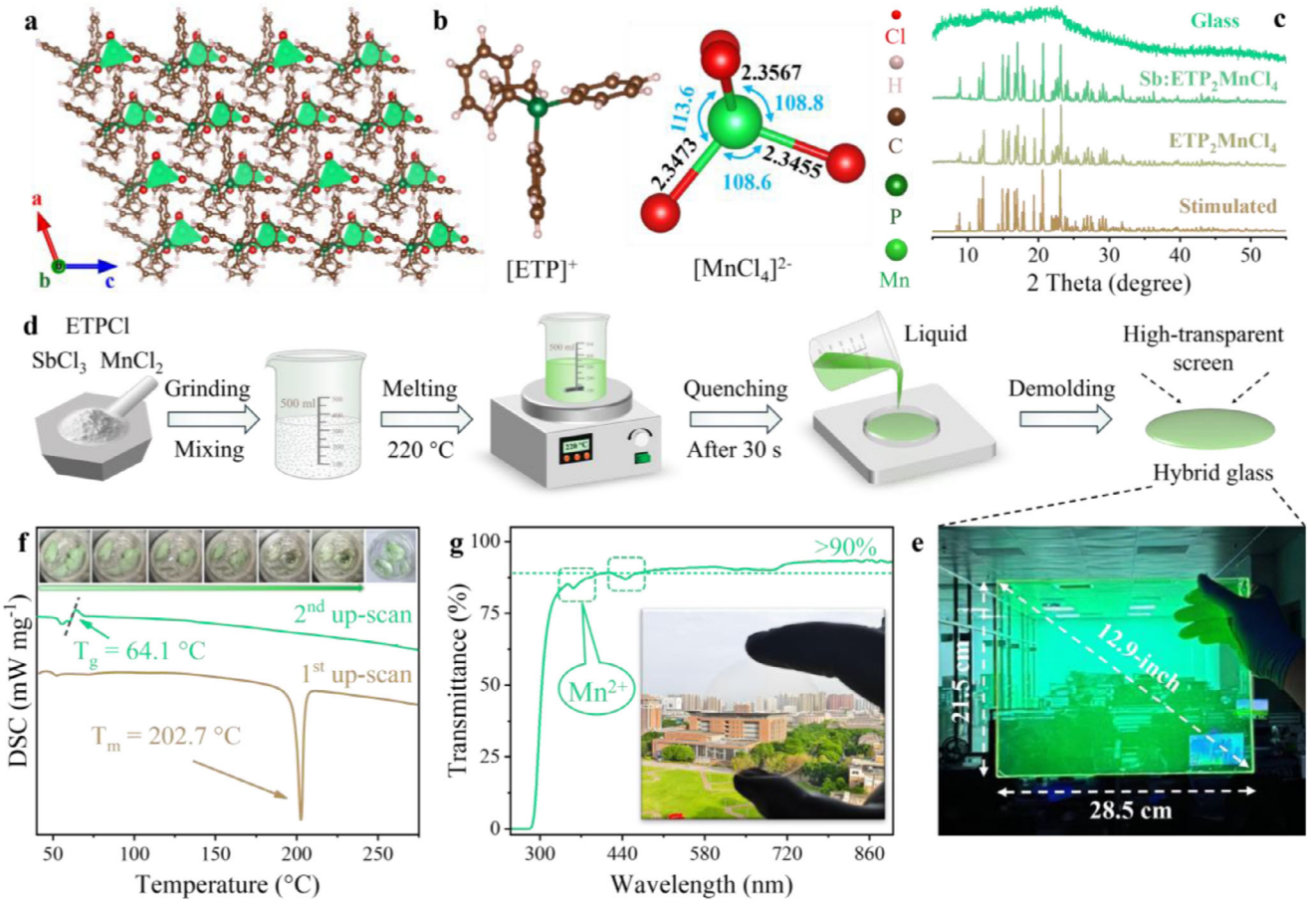

FIGURE 1 | Single-crystal structure and hybrid glass formation. (a) Crystal structure of ETP_2MnCl_4. (b) Organic cation ETP^+ and inorganic $[MnCl_4]^{2-}$ octahedron with the key bond lengths and angles. Units are Å. (c) XRD patterns of simulated ETP_2MnCl_4 crystal, Sb: ETP_2MnCl_4 crystal, and glass. (d) Preparation process of Sb: ETP_2MnCl_4 glass using ETPCl, $MnCl_2$, and $SbCl_3$. (e) Transparent sandwich-structured glass with a size of 28.5 × 21.5 cm^2 under UV light irradiation. (f) First up-scan and second up-scan DSC curves of Sb: ETP_2MnCl_4 crystal, demonstrating melting temperature (T_m = 202.7°C) and glass-transition temperature (T_g = 64.1°C). (g) Transmittance curve of Sb: ETP_2MnCl_4 glass. Insets of (f) and (g) show the melting state with elevation of temperature and the photograph of the glass, respectively.

growth or sintering procedures typically required for conventional inorganic scintillators. It also allows direct casting into flexible silicone molds, enabling customized flat, curved, or irregular scintillation screens with controllable thickness and geometry. Figure 1e presents a large-area Sb: ETP_2MnCl_4-based glass (28.5 × 21.5 cm^2), which exhibits uniform and intense luminescence together with high optical transparency under UV light excitation. To validate this approach, thermogravimetric (TG) and differential scanning calorimetry (DSC) measurements were performed on Sb: ETP_2MnCl_4 (Figure 1f; Figure S5a). The results reveal that Sb-doped ETP_2MnCl_4 single crystal possesses excellent thermal stability, with a melting point (T_m = 202.7°C, Figure 1f) well below the decomposition temperature (T_d = 309°C, Figure S5a). The mass loss at T_m is only 0.6%, confirming the ability to produce a stable melt, which is essential for preparing highly transparent glass via melt-quenching [21, 23–25]. The inset in Figure 1f illustrates the transformation from a crystalline state to a glassy one. The second up-scan DSC curve (Figure 1f) shows a clear heat capacity step, corresponding to a glass transition temperature (T_g) of 64.1°C. Based on the T_g and melting temperature, the T_g/T_m ratio was calculated to be approximately 0.71. This value indicates good glass-forming ability for the Sb: ETP_2MnCl_4 system and further supports the facile formation of transparent glass through melt-quenching. It is worth noting that TG and DSC measurements were conducted under a nitrogen atmosphere. In practical glass preparation, however, the melt is typically exposed to ambient environments with relative humidity above 70%. Under such conditions, both rapid quenching and natural cooling tend to yield green crystalline precipitates (Figure S5b), identified as Sb: ETP_2MnCl_4 (Figure S5c), being consistent with previous reports [23, 26].

To suppress the crystallization tendency during melt-quenching, introducing bulky organic cations with high steric hindrance has been widely recognized as an effective strategy in halide glass synthesis [27–29]. Accordingly, DPE-Phos, which exhibits a low T_m (187°C) and high T_d (318°C), was employed as a crystallization suppressor (Figure S6). Doping the Sb: ETP_2MnCl_4 melt with DPE-Phos enables direct air-quenching to yield stable, transparent glass. The PXRD pattern of the product displays a broad amorphous hump (Figure 1c), further confirming its glassy structure. Optical measurements demonstrate that the Sb: ETP_2MnCl_4 glass exhibits a high transmittance up to 92% in the 380–900 nm range (Figure 1g), exceeding those of previously reported hybrid metal halide glasses (Table S4). The transmission spectrum also shows characteristic Mn^{2+} absorption bands

(Figure S7a), validating the presence of Mn in the glass network. Moreover, this melt-quenching strategy is generalizable to other metal (B-site: Zn^{2+}, Sb^{3+}, Bi^{3+}) and organic (A-site: MTP^+, BTP^+) cations (Figure S7b). The exceptional optical transparency of Sb: ETP_2MnCl_4 glass effectively minimizes light scattering, a key advantage for optical devices, particularly in X-ray imaging [21, 27]. In comparison, the conventional scintillator screens composed of single crystals or polycrystalline powders embedded in binders such as silicone or epoxy will typically suffer from inevitable interfacial scattering (Figure S8).

To elucidate the impact of the crystal-to-glass transition on optical properties, we investigated the structure-property relationship of Sb: ETP_2MnCl_4 glass. Temperature-dependent in-situ XRD patterns reveal structural evolution from crystalline to amorphous. As shown in Figure 2a, several diffraction peaks disappear at 150°C, and further heating to 200°C yields a broad hump characteristic of an amorphous melt. This disordered structure was retained after quenching to room temperature, confirming the glassy state. Notably, the glass could be reconverted into a polycrystalline phase by thermal treatment (Figure S9a), indicating that the $[ETP]^+$ cations and $[MnCl_4]^{2-}$ tetrahedra confer high thermal stability to the framework. Fourier transform infrared (FTIR) spectra demonstrated that the melt-quenching process preserved the characteristic organic vibrational modes, including phenyl bending and C—H stretching (Figure 2b; Figure S9b). Raman spectra further confirmed the retention of the organic ETP^+ structure in the glass, with the low-frequency region clearly identifying the tetrahedral Mn—Cl vibrations (ν_1–ν_4, Figure 2c; Figure S9c) [18]. Notably, the Mn—Cl vibrational peaks in the glass exhibit pronounced broadening due to structural disorder. To probe the local coordination environment, X-ray absorption fine structure (XAFS) measurements were performed. The X-ray absorption near-edge structure (XANES) spectra at the Mn K-edge reveal similar coordination geometries in the glass and crystalline states, with absorption edge positions close to $MnCl_2$ (Figure 2d), confirming that Mn remains divalent. Fourier-transform fitting of the extended XAFS (EXAFS) indicates that the glass retains the Mn—Cl four-coordination with bond lengths consistent with those in the crystal (Figure 2e; Table S5). A minor Mn—O contribution was also detected, likely arising from trace water adsorption during air exposure [21]. Taken together, Sb: ETP_2MnCl_4 undergoes a crystalline-to-amorphous transformation during glass formation.

To demonstrate that organic cations and inorganic tetrahedra are largely preserved in glass, we performed ab initio molecular dynamics (AIMD) simulations on Sb: ETP_2MnCl_4 to visualize the crystal-to-glass transformation process. The melting was modeled using a canonical ensemble (NVT) with a constant volume, whereas the quenching process was simulated via a microcanonical ensemble [27, 30]. To mitigate the high computational cost associated with AIMD, the total simulation time was set to 10 picoseconds (ps), which is significantly shorter than the experimental melting timescale. Accordingly, the maximum simulation temperature was set to 2000 K, which is far above the actual melting point. The radial distribution function (RDF) offers an intuitive measure of interatomic distances by quantifying the probabilistic distribution of particles as a function of separation r. Specifically, RDFs derived for atomic pairs such as Mn—P, P—P, and Mn—Cl, as extracted from AIMD trajectories, reveal not only characteristic bond lengths but also the extent of long-range ordering. As depicted in Figure 2f,g, the distribution of P—P and Mn—P distances exhibits a marked broadening with elevation of temperature from 300 K to 2000 K, reflecting enhanced atomic thermal vibration and raised structural disorder. The generalized Lindemann ratio criterion [14, 31], commonly used to identify melting with a threshold of 15%, was evaluated based on the corresponding $G_{Mn-P}(r)$ and $G_{P-P}(r)$ profiles. The calculated ratio exceeds this value above 1200 K, confirming the transition to a molten state (Figure S10). In contrast, the Mn—Cl distance distribution remains essentially unchanged, suggesting the stability of $[MnCl_4]^{2-}$ tetrahedral units throughout the heating process (Figure 2h). The mean square displacement (MSD) derived from AIMD simulations indicates a substantial increase in atomic displacements at elevated temperatures (Figure 2i; Figure S11a,b), signifying the onset of liquid-like diffusive behavior [14, 27, 30]. This is marked by a steady rise in the diffusion coefficient with temperature (Figure S11c), culminating in pronounced diffusion at 2000 K (Movie S1), which characterizes the molten state of the system.

To elucidate the formation mechanism of the glassy phase, we conducted AIMD simulations in which the high-temperature melt at 2000 K was rapidly quenched to 300 K (Movie S2). The resulting glass exhibits an RDF that closely resembles that of the molten state, while the MSD gradually decreases with simulation time (Figure S12), indicating a progressive convergence of the disordered melt structure and the eventual formation of a glassy state with structural disorder. Although previous characterizations revealed that the glass and crystalline phases share similar local coordination for the inorganic $[MnCl_4]^{2-}$ tetrahedra and organic ETP^+ cations, their spatial arrangement in the glass exhibits substantially higher disorder (Figure 2j). The above microstructural analysis corroborates the superior performance of the transparent glass scintillation screen previously demonstrated, in which reduced optical scattering enables sharper and higher-resolution X-ray imaging compared to conventional polycrystalline screens.

As shown in Figure 3a, pristine ETP_2MnCl_4 crystal exhibits strong UV absorption band at 280 nm, together with characteristic Mn^{2+} d–d transitions between 340 nm and 500 nm assigned to 358 nm $^6A_1 \rightarrow {}^4T_1(P)$, 382 nm $^6A_1 \rightarrow {}^4E(D)$, 432 nm $^6A_1 \rightarrow {}^4E/{}^4A_1(G)$ and 446 nm $^6A_1 \rightarrow {}^4T_2(G)$. Upon Sb^{3+} incorporation, the absorption in the 310∼420 nm region is markedly intensified and broadened, attributable to $^1S_0 \rightarrow {}^3P_n$ transitions of Sb^{3+} ions with an ns^2 electronic configuration [32]. Under 283 nm excitation, undoped ETP_2MnCl_4 emits intense green luminescence at 520 nm with a 1.98 eV Stokes shift and a millisecond-scale lifetime of 1.32 ms (Figure 3b; Figure S13), being consistent with the $^4T_1(G) \rightarrow {}^6A_1$ transition of Mn^{2+} in $[MnCl_4]^{2-}$ tetrahedra. In contrast, the Sb-doped ETP_2MnCl_4 crystal displays an additional broadband emission centered at ∼694 nm, characterized by a large 2.55 eV Stokes shift and a 5.4 µs lifetime (Figure 3b; Figure S13). Excitation spectra monitored at different emission wavelengths reveal distinct profiles (Figure 3b; Figure S14a), confirming the coexistence of two independent radiative channels, with Mn^{2+} dominating in the 250–300 nm and 420–480 nm ranges and Sb^{3+} in the 350–450 nm range, reflecting their different absorption characteristics. This broadband deep-red emission, featuring a large Stokes shift and microsecond lifetime, is typical of self-

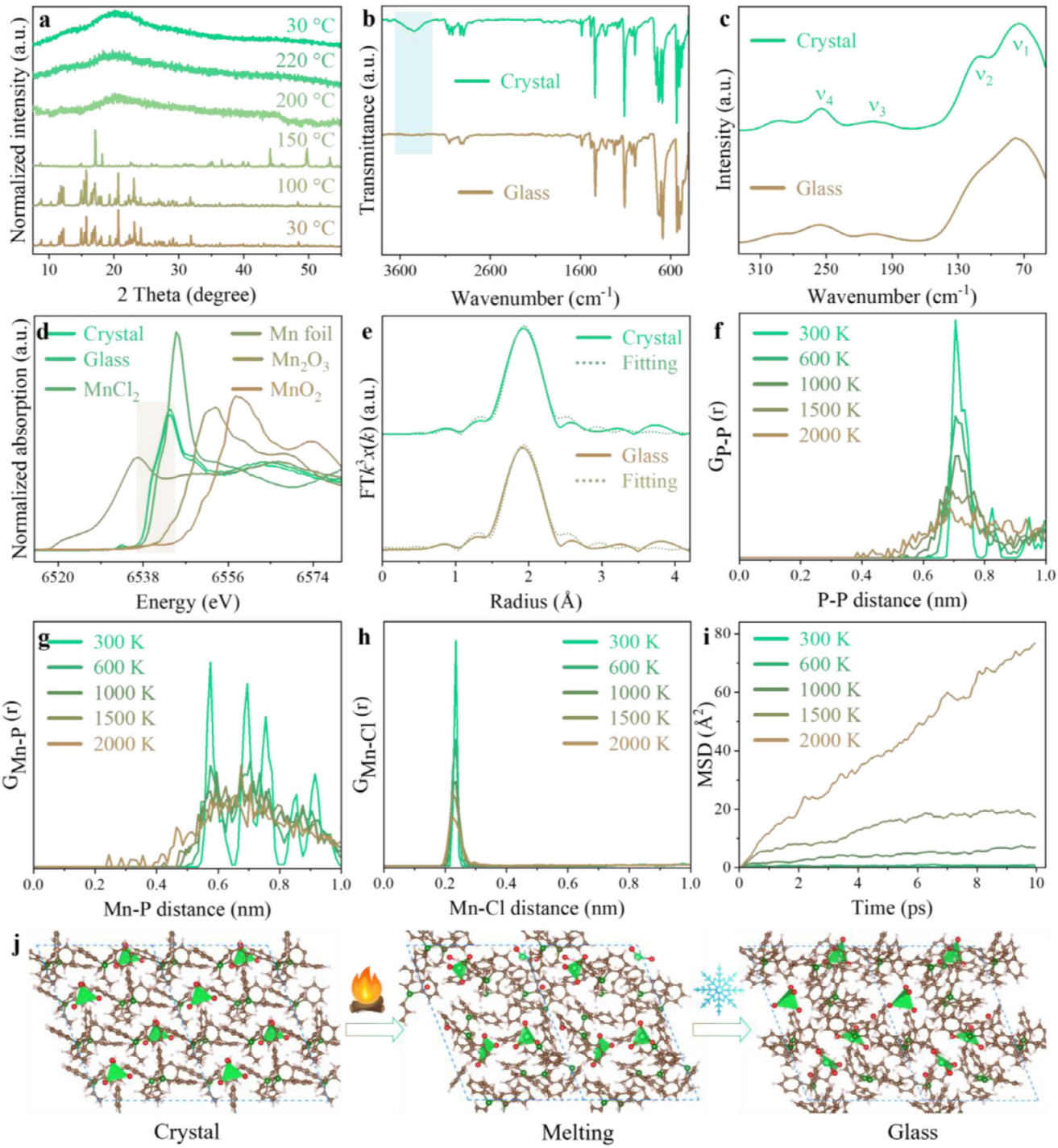

FIGURE 2 | Thermal-induced phase transition, optical performance, and AIMD simulations. (a) Temperature-dependent in-situ XRD patterns of Sb: ETP_2MnCl_4 crystal. (b) FTIR and (c) Raman spectra of Sb: ETP_2MnCl_4 crystal and glass. (d) Normalized XANES spectra at the Mn K-edge of Mn foil, $MnCl_2$, Mn_2O_3, MnO_2, Sb: ETP_2MnCl_4 crystal, and glass. (e) Fitting of Fourier-transformed EXAFS spectra at the Mn K-edge of Sb: ETP_2MnCl_4 crystal and glass. Partial RDF for (f) P–P, (g) Mn–P, and (h) Mn–Cl distances at various temperatures. (i) MSD of the P element vs. simulation time at various temperatures. (j) Molecular structures of the crystal at 300 K, the molten state at 2000 K, and the glassy state obtained by quenching from 2000 to 300 K.

trapped exciton (STE) emission in halide systems [33–35]. Unlike the common $[SbCl_5]^{2-}$ coordination observed in hybrid Sb(III) halides [36–39], Sb^{3+} ions in this system adopt a tetrahedral $[SbCl_4]^-$ coordination, leading to an overall redshift in excitation and emission (Figure S14b). As shown in Figure 3b and Figure S15a, the excitation spectrum of ETP_2MnCl_4 monitored at 520 nm closely matches the absorption of ETPCl, particularly overlapping with its 355 nm emission, suggesting an organic-to-inorganic energy transfer pathway. To verify this, we synthesized a series of $ETP_2Zn_{1-x}Mn_xCl_4$ crystals. With increasing Mn^{2+} content, both singlet fluorescence (350 nm) and triplet phosphorescence (490 nm) intensities progressively weaken, while Mn^{2+} emission

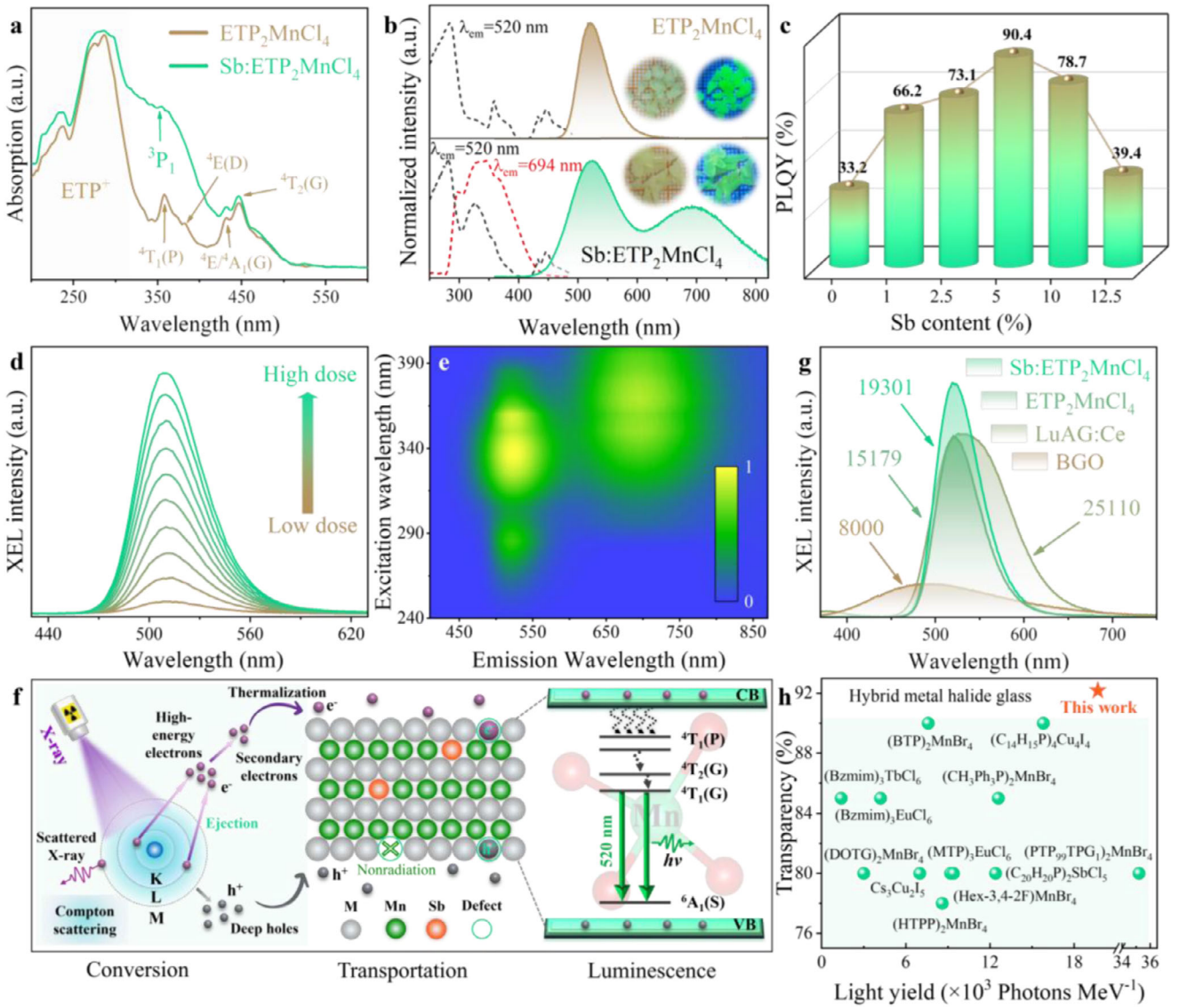

FIGURE 3 | Optical properties and luminescence mechanism of Sb: ETP2MnCl4. (a) Optical absorption spectra, (b) normalized PLE/PL spectra of ETP_2MnCl_4 and Sb: ETP_2MnCl_4 crystals. Inset: photographs under daylight and UV light irradiation, respectively. (c) PLQYs of Sb: ETP_2MnCl_4 crystals with different Sb^{3+} contents. (d) RL spectra of Sb: ETP_2MnCl_4 glass under different X-ray irradiation doses. (e) Excitation wavelength-dependent PL spectra of Sb: ETP_2MnCl_4 glass. (f) Emission mechanism of Sb:ETP_2MnCl_4 glass scintillator upon X-ray excitation. CB, conduction band; VB, valence band. (g) RL spectra of BGO, LuAG: Ce, ETP_2MnCl_4 glass, and Sb: ETP_2MnCl_4 glass. (h) Benchmark of reported light yields among representative transparent hybrid metal halide glass scintillators.

strengthens (Figure S15b). Correspondingly, the fluorescence lifetime shortens from 2.7 ns to 1.4 ns, and the phosphorescence lifetime remarkably decreases from 241.6 ms to 1.0 ms (Figure S15c–f), confirming energy transfer from the organic ligands to Mn^{2+} centers. In Sb: ETP_2MnCl_4, Sb^{3+} doping not only triggers STE-related broadband emission but also enhances Mn^{2+} emission (Figure S16a). Excitation spectra monitored at Mn^{2+} emission exhibit a ~330 nm peak matching the absorption profile (Figure S16b), indicating efficient energy transfer from Sb^{3+} excited states to Mn^{2+} energy levels. Simultaneously, substitution of $[MnCl_4]^{2-}$ units by $[SbCl_4]^-$ suppresses Mn^{2+}–Mn^{2+} aggregation. Temperature-dependent PL spectra and thermal activation energy analysis further demonstrate that $[SbCl_4]^-$ incorporation effectively reduces nonradiative processes, as evidenced by the increased activation energy from 74 meV in the ETP_2MnCl_4 crystal to 93 meV in the Sb: ETP_2MnCl_4 crystal (Figure S17). Collectively, the incorporation of Sb^{3+} significantly enhanced the room-temperature PLQY from 33.2% for the undoped crystals to 90.4% (Figure 3c). Ten replicate measurements yielded an average PLQY of 88.1%, confirming the reproducibility of this high value (Figure S17e,f). At 77 K, the PLQY further increased to 96.89% (Figure S17g). The original temperature-dependent PL intensity should not be directly scaled to estimate PLQY, because it is affected by both excitation absorption and intrinsic light-conversion efficiency. The absorbed-photon analysis reveals a higher fraction of absorbed excitation photons at low temperature, while the temperature-dependent PLE spectra (Figure S17h) show a concomitant enhancement in the excitation response. Together, these results explain why the low-temperature PL intensity increases more markedly than the PLQY. Moreover,

the broadband deep-red emission of the Sb: ETP_2MnCl_4 crystal exhibits strong electron-phonon coupling with a Huang–Rhys factor (S) as high as 32.5, further substantiating its origin from the formation of the STE state (Figure S18).

Based on these findings, we propose a dual-channel cooperative enhanced PL mechanism for Sb: ETP_2MnCl_4 (Figure S19). In ETP_2MnCl_4, UV light excitation promotes electrons in organic chromophores from the S_0 ground state to excited states, which rapidly relax to the lowest S_1 state via ultrafast internal conversion. A fraction of these carriers undergo radiative relaxation to yield singlet fluorescence, while others undergo intersystem crossing (ISC) to the triplet state (T_n), followed by energy transfer to Mn^{2+} centers, yielding green emission via the $^4T_1(G)\rightarrow{}^6A_1$ transition. Upon Sb^{3+} doping, additional UV absorption and subsequent dual pathways emerge: (i) energy transfer from Sb^{3+} to Mn^{2+} enhances green emission, while (ii) Sb^{3+} excitons self-trap to produce broad deep-red STE emission. Concurrently, $[SbCl_4]^-$ incorporation alleviates Mn^{2+} clustering, leading to the further enhancement of luminescence efficiency. Notably, after converting from the crystal into an amorphous state, the Sb: ETP_2MnCl_4 glass displays excitation and emission behaviors nearly identical to those of the crystalline counterpart (Figure S20a), which is due to the well preservation of $[MnCl_4]^{2-}$ tetrahedra and ETP^+ ligand in glass. Time-resolved PL spectra reveal a slightly shortened decay lifetime after crystal-to-glass transformation (Figure S20b), accompanied by a decrease in PLQY from 90.4% (crystal) to 62.5% (glass) (Figure S20c,d). This degradation is intrinsic and primarily arises from increased structural disorder, which lowers the overall rigidity of the system and promotes nonradiative recombination pathways.

Interestingly, X-ray-excited dose-dependent RL spectra reveal that the glass exhibits almost exclusively the characteristic Mn^{2+} emission (Figure 3d), while the Sb^{3+}-related STE signal completely disappears, distinctly different from its PL behavior. To further probe this behavior, excitation-wavelength-dependent PL mapping was collected (Figure 3e). The results show that both Mn^{2+} and STE emissions appear in the low-energy excitation region, whereas only Mn^{2+} emission persists under high-energy excitation (<290 nm), consistent with the spectral response under X-ray excitation. To verify the origin of the missing STE signal, Mn-free ETP_2SbCl_5 was examined and displayed clear STE emission under X-ray excitation (Figure S21). These findings indicate that, under high-energy or X-ray excitation, the energy absorbed by Sb^{3+} will be transferred to Mn^{2+} rather than STE. Two primary mechanisms underpin this behavior. First, the enhanced mobility of hot carriers under high-energy excitation increases their probability of encountering and being trapped by the high-content Mn^{2+} in Sb: ETP_2MnCl_4, outcompeting the localization process needed for STE formation. Second, the relatively long excited-state lifetime of STEs makes this channel susceptible to saturation, so that rapid energy transfer from Sb^{3+} to Mn^{2+} becomes the dominant relaxation route for excess carriers. Based on these observations, we propose an energy transfer and RL mechanism under X-ray excitation, as illustrated in Figure 3f. Incident X-ray photons first interact with heavy elements through photoelectric absorption and Compton scattering [3, 5], producing large numbers of energetic carriers. These carriers rapidly thermalize, generating numerous secondary electrons/holes that subsequently create low-energy electron-hole pairs via collisional ionization. Ultimately, the carriers relax to the lowest excited state of Mn^{2+} ion, giving rise to characteristic green luminescence. Importantly, Sb^{3+} dopants act as both efficient energy-transfer mediators—channeling excitation energy into Mn^{2+} centers—and as structural modifiers, substituting $[MnCl_4]^{2-}$ units with $[SbCl_4]^-$ to suppress Mn^{2+} clustering [37, 40], thereby further enhancing RL efficiency. Under identical dose conditions, the X-ray excited luminescence (XEL) intensity of ETP_2MnCl_4 glass surpasses that of commercial BGO and is further boosted upon Sb doping (Figure 3g). Using BGO (8000 photons·MeV^{-1}) as a reference, the Sb: ETP_2MnCl_4 glass achieves a remarkable light yield of 19,301 photons·MeV^{-1}, validated by cross-comparison with LuAG: Ce (25,000 photons·MeV^{-1}). The specific calculation process and test details are described in the *Experimental Section*. Figure 3h benchmarks the reported light yields among transparent hybrid metal halide glass scintillators, while Table S4 separately summarizes the transmittance, detection limit, spatial resolution, and screen size of representative systems. It should be noted that optical transparency and light yield are related but not equivalent descriptors: the former governs photon transport and suppresses lateral light spreading in scintillation screens, whereas the latter reflects the overall scintillation output. Indeed, several previously reported transparent hybrid glass scintillators still exhibit relatively modest light yields, such as $Bzmim_3(Tb/Eu)Cl_6$ glasses (>85% transmittance; 4101/1419 photons·MeV^{-1}), $(DOTG)_2MnBr_4$ glass (>80% transmittance; 3000 photons·MeV^{-1}), and $(1\text{-}Bz\text{-}3\text{-}PhPy)_2MnBr_4$ glass (>80% transmittance; 7590 photons·MeV^{-1}) [23, 41, 42]. In this context, the Sb: ETP_2MnCl_4 glass distinguishes itself by simultaneously delivering >92% transparency, a light yield of 19,301 photons·MeV^{-1}, and a spatial resolution of 30.1 lp·mm^{-1}, highlighting its promise for high-performance X-ray imaging.

Another remarkable advantage of Sb: ETP_2MnCl_4 hybrid glass is its intrinsic self-healing and reshaping capability (Process *1* in Figure 4a). Mechanical damage can be repaired at ~220°C, which is far below the repair temperature of all-inorganic glasses (>800°C) [1, 43], and the luminescence remains unchanged over 10 consecutive damage-repair cycles (Figure 4b,c). Beyond mechanical self-healing, the glass could be reversibly transformed into crystalline powder with yields up to 90% via ethanol-assisted recrystallization (Processes *2, 3* in Figure 4a,d). This reversible glass-crystal transition is highly tolerant: Even after 12 transformation cycles, the reshaped glass exhibits negligible variation in optical performance (Figure 4e; Figure S22a,b). Such recyclability not only provides a practical pathway for resource recovery and reuse of glass scintillators but also ensures that the material retains value even when damaged or at the end of its service lifetime. We further assessed the long-term environmental stability of Sb: ETP_2MnCl_4 glass. Without protection, minor recrystallization appeared after 15 days of air exposure and became more pronounced after 30 days (Figure S22c), likely due to ambient humidity [27, 30, 44]. To enhance atmospheric durability, we fabricated a sandwich-structured transparency glass by quenching the molten material between two quartz plates. This encapsulated glass maintained essentially unchanged transmittance and PLQY after being placed in air for 30 days (Figure 4f; Figure S22d), and exhibited good resistance to mechanical impact. This strategy not only improves atmospheric durability but also imparts additional mechanical robustness, offering a viable route toward practical application of scintillating glasses.

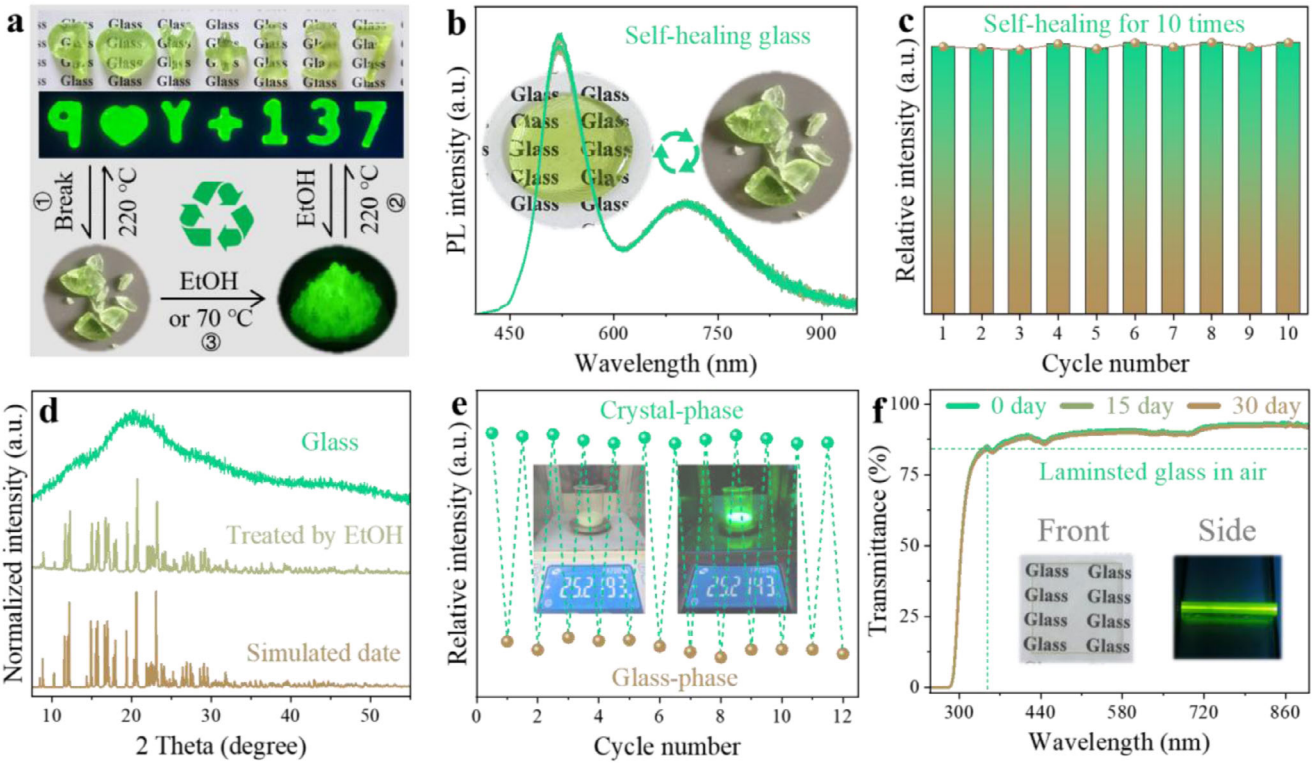

FIGURE 4 | Self-healing and recyclable repurposing. (a) Schematic diagram for reversible phase transition between crystal and glass. (b) PL spectra and (c) the corresponding integrated intensities of Sb: ETP_2MnCl_4 glass via self-healing for 10 cycles. (d) XRD patterns for the products obtained by the reverse phase transition from Sb: ETP_2MnCl_4 glass. (e) Integrated PL intensities of the products by the phase transition between crystal and glass for 12 cycles. The inset of (e) is the photograph of recycled Sb: ETP_2MnCl_4 in mass production. (f) Transmittance spectra of the sandwich-structured Sb: ETP_2MnCl_4 glass at 0, 15, and 30 days. Inset: Corresponding photographs from the front and side.

Subsequently, we evaluated the X-ray absorption capability and operational stability of highly transparent Sb: ETP_2MnCl_4 glass scintillators. As shown in Figure 5a, Sb: ETP_2MnCl_4 exhibits absorption comparable to Si across a broad photon-energy range, owing to the presence of heavy atoms (Sb, Mn, and Cl), while markedly outperforming typical organic scintillators such as tetraphenylethylene (TPE). Remarkably, a 1-mm-thick Sb: ETP_2MnCl_4 layer achieves complete X-ray absorption at 8 keV (Figure S23a). Under X-ray excitation, the glass displays an excellent linear RL response over a wide dose-rate range (Figure 5b), with a sensitivity surpassing not only ETP_2MnCl_4 glass but also conventional BGO, highlighting its potential in both dosimetry calibration and high-contrast imaging. Thermal activation analysis reveals that the activation energies under both X-ray and UV light excitation reach 127 meV and 93 meV, respectively (Figure 5c). Such high thermal activation energies ensure inhibited non-radiative recombination loss at high temperatures, leading to highly stable Mn^{2+} PL&RL for the present glass sample.

Moreover, the scintillator achieves an exceptionally low X-ray detection limit of 82.3 $nGy_{air}\cdot s^{-1}$ at a signal-to-noise ratio of 3 (Figure S23b), nearly 67-fold lower than the clinical diagnostic threshold of 5500 $nGy_{air}\cdot s^{-1}$, highlighting its capacity to minimize radiation exposure. The Sb: ETP_2MnCl_4 glass also demonstrates outstanding radiation stability under prolonged X-ray irradiation. Even under combined exposure to X-rays and an elevated temperature (80°C), its luminescence intensity shows negligible alteration (Figure 5d). Stable XEL intensity was maintained over 60 consecutive on/off cycles (Figure 5e), confirming excellent operational durability and radiation resistance.

All X-ray imaging measurements, including the line-pair-card test, were conducted under light-tight conditions using a detector with a camera pixel size of 4.35 μm, an X-ray dose rate of 34.8 $mGy_{air}\ s^{-1}$, a voltage of 50 kV, and an exposure time of 30 s, corresponding to an integrated dose of 1044 mGy_{air}. To evaluate the possible optical bright-field contribution arising from the scintillator emission, two imaging configurations were compared. In the contact-coupled configuration, the line-pair card was placed directly against the transparent sandwich-structured Sb: ETP_2MnCl_4 glass scintillator. In the optical-barrier configuration, a thin black cardstock was inserted between the line-pair card and the scintillator to prevent the green scintillation emission (≈530 nm) from optically illuminating the card. All other X-ray irradiation and image-acquisition parameters were kept unchanged. Under both configurations, the line-pair features at 20.0 $lp\cdot mm^{-1}$, corresponding to the highest spatial frequency available on the line-pair card, remained clearly distinguishable, as confirmed by the corresponding periodic gray-value profiles (Figure 5f; Figure S23c). The modulation transfer function (MTF) curves were calculated from X-ray-excited scintillation images using the slanted-edge method (Figure 5f). At an MTF value of 0.2, the limiting spatial resolutions were determined to be 31.4 and 30.1 $lp\cdot mm^{-1}$ for the contact-coupled and optical-barrier configurations, respectively. The minor difference indicates that the scintillator-emission-induced optical contribution has a neg-

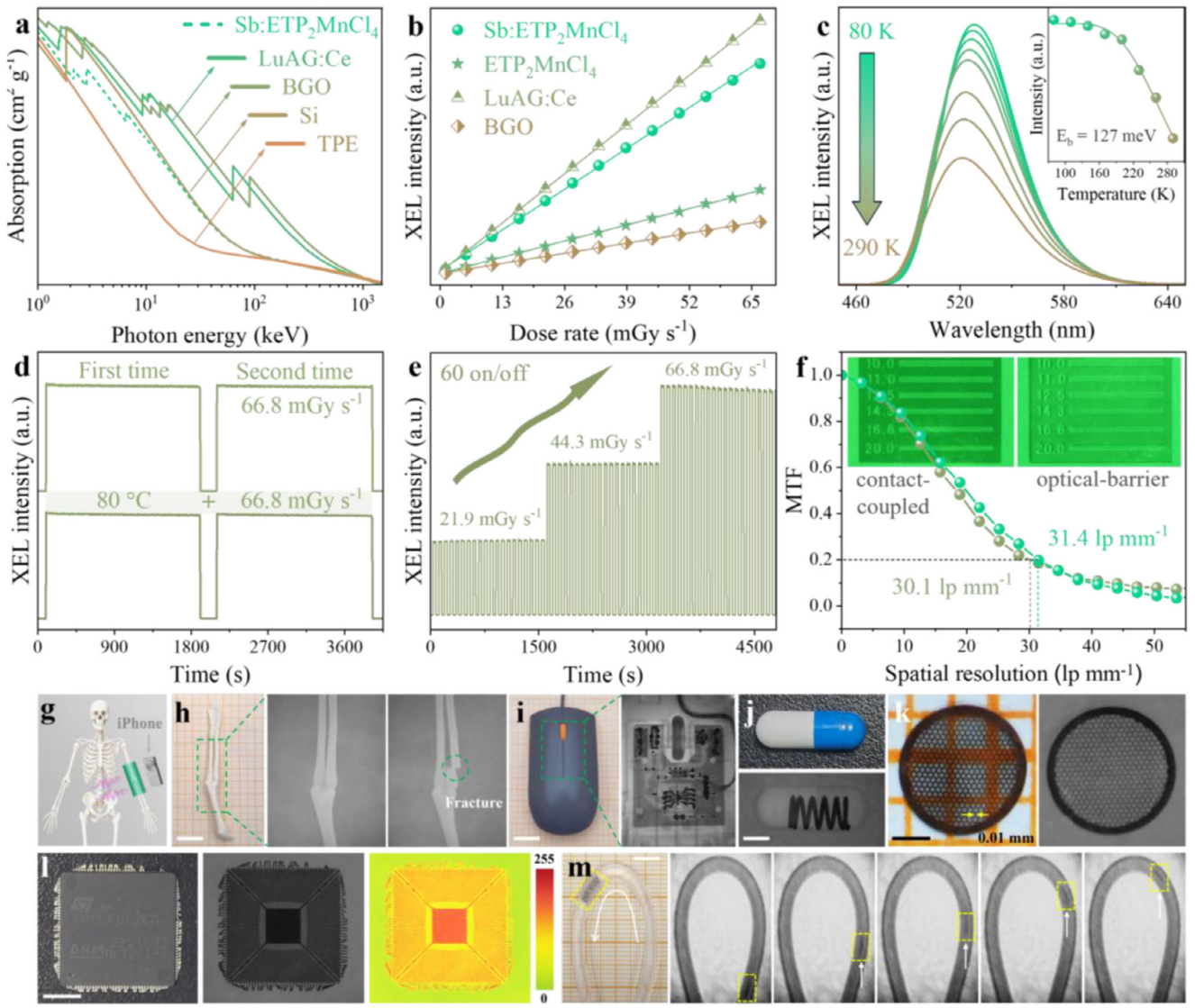

FIGURE 5 | Scintillation performance and X-ray imaging of glass scintillation. (a) Absorption coefficients of TPE, Si, LuAG: Ce, BGO, and Sb: ETP_2MnCl_4 as a function of photon energy. (b) XEL intensity of BGO, LuAG: Ce, ETP_2MnCl_4 glass, and Sb: ETP_2MnCl_4 glass as a function of dose rate. (c) Temperature-dependent RL spectra of Sb: ETP_2MnCl_4 glass. Inset: Temperature-dependent XEL intensity of Mn^{2+} emission to evaluate thermal activation energy. (d) RL stability of Sb: ETP_2MnCl_4 glass under X-ray irradiation and at 80°C with X-ray working (66.8 mGy s^{-1}, voltage: 20 kV). (e) RL stability of Sb: ETP_2MnCl_4 glass scintillator recorded over 60 on/off cycles (dose rate: 21.9, 44.3, 66.8 mGy s^{-1}, voltage: 20 kV). (f) MTF curves of the Sb: ETP_2MnCl_4 glass scintillator obtained under the contact-coupled and optical-barrier configurations using the slanted-edge method. Insets: corresponding X-ray images of the line-pair card showing clearly resolved features at 20.0 lp·mm^{-1}. (g) Schematic diagram of X-ray imaging system captured with a mobile phone. (h) Skeleton photos taken by the mobile phone (scale bars: 2 cm). Photographs and static X-ray images of the (i) mouse (scale bars: 2 cm), (j) spring (scale bars: 1 cm), and (k) copper mesh (scale bars: 1 mm) under daylight and X-ray irradiation. (l) Photographs of an electronic device (left), gray (middle), and colorful (right) X-ray scintillation images. Scale bars: 5 mm. (dose rate: 21.9, 44.3, 66.8 mGy s^{-1}, voltage: 20 kV) (m) Schematic and intercepted photographs from real-time X-ray image simulating high-speed angiography (scale bars: 1 mm; time interval: 6 ms).

ligible influence on the measured spatial resolution under the present conditions. The spatial resolution of 30.1 lp·mm^{-1} obtained in the optical-barrier configuration still exceeds those of BGO (11 lp·mm^{-1}) and CsI:Tl (10 lp·mm^{-1}) [3], and outperforms most previously reported hybrid metal halide glass scintillators (Table S4).

Recently, owing to their portability and operational flexibility, smartphone-based health platforms have emerged as a promising alternative to conventional radiological diagnostics, which rely on bulky equipment and specialized facilities. To demonstrate the applicability of Sb: ETP_2MnCl_4 glass-scintillation screens in such portable systems, we integrated a 12.9-inch glass screen with a smartphone camera (Figure 5g). The smartphone directly captured X-ray images of clinically relevant targets, such as bone fractures, enabling rapid and accessible diagnostics (Figure 5h). Beyond clinical use, the glass screens delivered high-resolution X-ray images of various objects, including a mouse, spring, card reader, and fish specimen, all of which displayed clear internal features (Figure 5i,j; Figure S24). Fine structures down to

0.02 mm line width were resolved on a copper mesh (Figure 5k), underscoring their capability for microscale imaging. To further enhance interpretability, grayscale images were converted into RGB (Red, Green, Blue) maps through a color-reconstruction strategy, which sharpened edges and improved structural visibility without loss of resolution (Figure 5l). This approach can be extended to 3D reconstructions, enabling detailed visualization of complex, multi-material systems. In addition to static imaging, the screens supported dynamic monitoring: a vascular phantom with circulating fluid reproduced high-speed angiography for blood-flow-pattern analysis relevant to the diagnosis of tumors and vascular blockages, while the trajectory of a tungsten-steel sphere (1 mm diameter) was tracked at 60 fps (Figure 5m; Movie S3). Taken together, these results establish the Sb: ETP_2MnCl_4 glass scintillators as multifunctional platforms that combine high spatial and temporal resolution, offering precise structural imaging and real-time target tracking. Their portability and versatility highlight broad potential for next-generation medical diagnostics and industrial nondestructive testing.

3 | Conclusion

In summary, we have developed a large-area (21.5 × 28.5 cm^2), highly transparent (92%) Sb: ETP_2MnCl_4 hybrid halide glass scintillator that unites a high light yield of 19,301 photons·MeV^{-1}, an ultralow detection limit of 82.3 $nGy_{air}·s^{-1}$, and a high spatial resolution of 30.1 lp·mm^{-1} with unprecedented recyclability and processability. Unlike conventional commercial or perovskite scintillators, the material leverages organic-inorganic hybrid design and Sb^{3+} engineering to achieve efficient dual-channel luminescence, robust Mn^{2+}-based radioluminescence, and scalable screen fabrication. Its self-healing, low-temperature reshaping, and reversible crystal-glass transitions not only provide practical strategies for sustainable reuse but also introduce a new paradigm for functional glass design. Coupled with smartphone-based X-ray imaging, the multifunctionality of Sb: ETP_2MnCl_4 scintillators bridges fundamental photophysics and real-world applications. This work thus establishes hybrid halide glasses as a transformative class of eco-friendly scintillators with broad implications for medical diagnostics, nondestructive testing, and radiation detection technologies.

Acknowledgements

This research was supported by the National Natural Science Foundation of China (52572155 and 52272141) and the Natural Science Foundation of Fujian Province (2024J02014).

Conflicts of Interest

The authors declare no conflicts of interest.

Data Availability Statement

The data that support the findings of this study are available from the corresponding author upon reasonable request.

References

1. H. Zhang, X. Huang, T. Wan, et al., "Integrated Copper-Halide Activated Scintillator Fiber Array for Remote High-Resolution X-ray Imaging," *Nature Communications* 16 (2025): 5973, https://doi.org/10.1038/s41467-025-61416-7.

2. J. Fan, H. Li, W. Liu, and G. Ouyang, "Fabrication Strategies of Mn^{2+}-Based Scintillation Screens for X-Ray Detection and Imaging," *Angewandte Chemie* 137 (2025): 202425661.

3. T. Wang, G. Zeng, Y. M. Yang, et al., "Advances in Metal Halide Perovskite Scintillators for X-Ray Detection," *Nano-Micro Letters* 17 (2025): 275, https://doi.org/10.1007/s40820-025-01772-7.

4. B. J. Kim, B. Shao, A. T. Hoang, et al., "A Flexible Active-Matrix X-ray Detector with a Backplane Based on Two-Dimensional Materials," *Nature Electronics* 8 (2025): 147–156.

5. L. Xu, P. Ran, W. Zhou, et al., "All-Inorganic Metafabric Scintillators for Conformally Flexible and Wearable X-ray Detection and Imaging," *Science Advances* 11 (2025): adv5537, https://doi.org/10.1126/sciadv.adv5537.

6. M. Wang, Z. Zhang, J. Lyu, et al., "Overcoming Thermal Quenching in X-Ray Scintillators Through Multi-Excited State Switching," *Angewandte Chemie International Edition* 63 (2024): 202401949.

7. X. Du, S. Zhao, L. Wang, et al., "Efficient and Ultrafast Organic Scintillators by Hot Exciton Manipulation," *Nature Photonics* 18 (2024): 162–169, https://doi.org/10.1038/s41566-023-01358-y.

8. S. Y. Yang, L. Zhang, F. C. Kong, et al., "Scintillators With Aggregation-Induced Emission," *Chemistry* 11 (2025): 102534, https://doi.org/10.1016/j.chempr.2025.102534.

9. Z. Yang, J. Cui, Y. Sun, J. Yao, S. Yang, and J. Song, "Na-alloy Tailored 3D/0D Metal Halide Heterostructures Enabling Efficient Charge Transfer for Color-Integrated White Scintillators," *Nature Communications* 16 (2025): 6909, https://doi.org/10.1038/s41467-025-62195-x.

10. J. Li, K. Liao, J. Zhang, and F. Yuan, "High-Efficiency Ultra-broadband Warm White Light Emission From a Single-Component Lead-Free Perovskite With Record-Low Blue-Violet Content," *Advanced Functional Materials* 36 (2025): 12240, https://doi.org/10.1002/adfm.202512240.

11. C. Li, L. Wang, D. Tu, et al., "Luminescence Lifetime Thermometers Based on Hybrid Cuprous Halides With Exceptional Water Resistance and Giant Thermal Expansion," *Light: Science & Applications* 14 (2025): 224, https://doi.org/10.1038/s41377-025-01910-1.

12. L. Li, J. Jin, K. Han, Y. Wang, and Z. Xia, "Rational Design and Synthesis of Narrow-Band Emitting Eu(II)-Based Hybrid Halides via Alkyl Thermal Cleavage," *Nature Communications* 16 (2025): 7479, https://doi.org/10.1038/s41467-025-62748-0.

13. J. Xu, R. Luo, Z. Luo, et al., "Ultrabright Molecular Scintillators Enabled by Lanthanide-assisted Near-Unity Triplet Exciton Recycling," *Nature Photonics* 19 (2025): 71–78, https://doi.org/10.1038/s41566-024-01586-w.

14. Y. Wen, Y. Xu, X. Zhang, et al., "Phase Control via Composite Encapsulation for Ultra-Stable, High-Resolution Organic Manganese Halide Scintillator Array," *Advanced Materials* 37 (2025): 07021, https://doi.org/10.1002/adma.202507021.

15. J. H. Chen, J. B. Luo, Q. P. Peng, Z. L. He, J. H. Wei, and D. B. Kuang, "Branched Alkyl Chains Tunable Organic-Inorganic Hybrid Manganese Halides for Anti-Counterfeiting, White Light-Emitting Diode and X-Ray Imaging Applications," *Angewandte Chemie International Edition* 64 (2025): 202508536, https://doi.org/10.1002/anie.202508536.

16. B. Li, Y. Sun, Y. Wang, et al., "Hybrid Cu (I)-Based Glassy Cluster Gel Scintillator Film by in Situ UV Photopolymerization," *Matter* 8 (2025): 102214.

17. Q. P. Peng, Z. L. He, J. H. Chen, et al., *Matter* 8 (2025): 10277.

18. B. Li, Y. Wang, Y. Xu, and Z. Xia, "Emerging 0D Hybrid Metal Halide Luminescent Glasses," *Advanced Materials* 37 (2025): 2415483, https://doi.org/10.1002/adma.202415483.

19. S. Wang, S. Chen, T. Pang, et al., "Topology Engineering of Red Perovskite Quantum Dots Glasses: A Path to Display With Rec.2020

Standard," *Laser & Photonics Reviews* 19 (2025): 00550, https://doi.org/10.1002/lpor.202500550.

20. F. Nie and D. Yan, "Zero-Dimensional Halide Hybrid Bulk Glass Exhibiting Reversible Photochromic Ultralong Phosphorescence," *Nature Communications* 15 (2024): 5519, https://doi.org/10.1038/s41467-024-49886-7.

21. Z. L. He, J. B. Luo, J. H. Chen, et al., "A Universal Strategy toward Two-Component Organic-Inorganic Metal Halide Luminescent Glasses and Glass-Crystal Composites," *Science Advances* 11 (2025): adu1982.

22. W. Zhang, W. Zheng, L. Li, et al., "Unlocking the Potential of Organic-Inorganic Hybrid Manganese Halides for Advanced Optoelectronic Applications," *Advanced Materials* 36 (2024): 2408777, https://doi.org/10.1002/adma.202408777.

23. T. C. Wang, Z. L. He, J. B. Luo, et al., "Organic–Inorganic Hybrid Rare Earth Halide Glasses for Tunable Multicolor X-Ray Scintillation," *Angewandte Chemie International Edition* 64 (2025): 202504658, https://doi.org/10.1002/anie.202504658.

24. C. Dong, X. Song, B. E. Hasanov, et al., "Organic–Inorganic Hybrid Glasses of Atomically Precise Nanoclusters," *Journal of the American Chemical Society* 146 (2024): 7373–7385, https://doi.org/10.1021/jacs.3c12296.

25. A. Singh and D. B. Mitzi, "Emergence of Melt and Glass States of Halide Perovskite Semiconductors," *Nature Reviews Materials* 10 (2025): 211–227, https://doi.org/10.1038/s41578-024-00759-x.

26. K. Liu, Y. Luo, Y. Jin, et al., "Moisture-Triggered Fast Crystallization Enables Efficient and Stable Perovskite Solar Cells," *Nature Communications* 13 (2022): 4891, https://doi.org/10.1038/s41467-022-32482-y.

27. Z. Zhou, J. Zheng, S. Ruan, et al., "A Transparent Hybrid Metal Halide Glassy Scintillation Screen for High-Resolution Fast Neutron Radiography," *Nature Communications* 16 (2025): 6215, https://doi.org/10.1038/s41467-025-61503-9.

28. W. L. Xue, G. Q. Li, H. Chen, et al., "Melt-Quenched Glass Formation of a family of Metal-Carboxylate Frameworks," *Nature Communications* 15 (2024): 2040, https://doi.org/10.1038/s41467-024-46311-x.

29. C. Zhao, Y. Wang, S. Bao, Y. Zang, X. Liu, and W. Huang, "High-Performance Hybrid Organic-Inorganic Lanthanide Halide Glass Scintillators Enabled by Dehydration for Efficient X-Ray Imaging," *Advanced Materials* 37 (2025): 2500925, https://doi.org/10.1002/adma.202500925.

30. H. Yang, H. Lu, X. Wang, et al., "Recyclable Luminescent Solar Concentrator From Lead-Free Perovskite Derivative," *Light: Science & Applications* 14 (2025): 297, https://doi.org/10.1038/s41377-025-01973-0.

31. R. Gaillac, P. Pullumbi, K. A. Beyer, et al., "Liquid Metal–Organic Frameworks," *Nature Materials* 16 (2017): 1149–1154, https://doi.org/10.1038/nmat4998.

32. W. Yang, P. Dang, G. Zhang, et al., "Multimode Luminescence Tailoring in PMA_4 $Na(In,Sb)Cl_8$ Organic–Inorganic Hybrid Metal Halide via Rigid Benzene Ring Induced Local Lattice Distortion," *Angewandte Chemie International Edition* 63 (2024): 202411136, https://doi.org/10.1002/anie.202411136.

33. H. Peng, X. Kan, W. Huang, et al., "Efficient Tunable White Emission and Blue Light-Excited Near-Infrared Emission in Lead-Free Metal Halide Crystals With Ultra-High Luminous Efficiency for Multispectral Image Fusion and 3D Image Reconstruction," *Advanced Functional Materials* 35 (2025): 2422115, https://doi.org/10.1002/adfm.202422115.

34. Y. Liu, F. Di Stasio, C. Bi, et al., "Near-Infrared Light Emitting Metal Halides: Materials, Mechanisms, and Applications," *Advanced Materials* 36 (2024): 2312482, https://doi.org/10.1002/adma.202312482.

35. D. Liu, P. Dang, G. Zhang, H. Lian, G. Li, and J. Lin, "Near-Infrared Emitting Metal Halide Materials: Luminescence Design and Applications," *InfoMat* 6 (2024): 12542.

36. S. Yu, H. Peng, Q. Wei, et al., "Realizing Efficient Broadband Near-Infrared Emission and Multimode Photoluminescence Switching via Coordination Structure Modulation in Sb^{3+}-Doped 0D Organic Metal Chlorides," *Materials Horizons* 11 (2024): 2230–2241, https://doi.org/10.1039/D3MH01962D.

37. H. Peng, S. Yu, Q. Wei, et al., "Efficient Broadband Near-Infrared Emitters in Lead-Free Metal Halides With Record Photoluminescence Quantum Yield Under Blue Light Excitation," *Advanced Functional Materials* 34 (2024): 2411807, https://doi.org/10.1002/adfm.202411807.

38. Q. Ren, G. Zhou, Y. Mao, N. Zhang, J. Zhang, and X. M. Zhang, "Optical Activity Levels of Metal Centers Controlling Multi-Mode Emissions in Low-Dimensional Hybrid Metal Halides for Anti-Counterfeiting and Information Encryption," *Chemical Science* 15 (2024): 16536–16545, https://doi.org/10.1039/D4SC05041J.

39. W. Chu, Z. Ma, Q. Zhou, et al., "Tailor-Made Host–Guest Organic–Inorganic Hybrid Antimony Halide Enables Efficient Light-Emitting Diodes," *Angewandte Chemie International Edition* 64 (2025): 202513452, https://doi.org/10.1002/anie.202513452.

40. T. Huang, Z. Wang, T. Li, et al., "Multifunctional Phosphor With High-Efficient Near-Infrared Emission Based on Antimony–Zinc Halides," *ACS Applied Materials & Interfaces* 16 (2024): 31322–31331, https://doi.org/10.1021/acsami.4c04622.

41. Z. L. He, J. H. Wei, J. B. Luo, et al., "Guanidinium-Based Manganese(II) Bromide With High Glass-Forming Ability for Thermoplastic Curved X-Ray Imaging," *Laser & Photonics Reviews* 18 (2024): 2301249, https://doi.org/10.1002/lpor.202301249.

42. Z. L. He, Y. X. Luo, J. H. Chen, et al., "Molecular Design-Enabled Pyridinium-Based Metal Halide Glass Scintillators With Robust Glass-Forming Ability and Tailorable Radioluminescence," *Angewandte Chemie* 137 (2025): 202518282, https://doi.org/10.1002/ange.202518282.

43. D. Hu, S. Lin, T. Pang, et al., "Ultra-Narrowband Green-Emitting Transparent Composite Ceramics for Laser-Driven Display," *Advanced Materials* 37 (2025): 2414957, https://doi.org/10.1002/adma.202414957.

44. X. Wang, X. Zhang, J. Wei, et al., "Flexible Hybrid Glass fiber With Low Optical Loss for X-ray Tracking," *Laser & Photonics Reviews* 19 (2025): 01008.

Supporting Information

Additional supporting information can be found online in the Supporting Information section.

Supporting File 1: lpor71787-sup-0001-SuppMat.docx.

Supporting File 2: lpor71787-sup-0002-MovieS1.mp4.

Supporting File 3: lpor71787-sup-0003-MovieS2.mp4.

Supporting File 4: lpor71787-sup-0004-MovieS3.mp4.